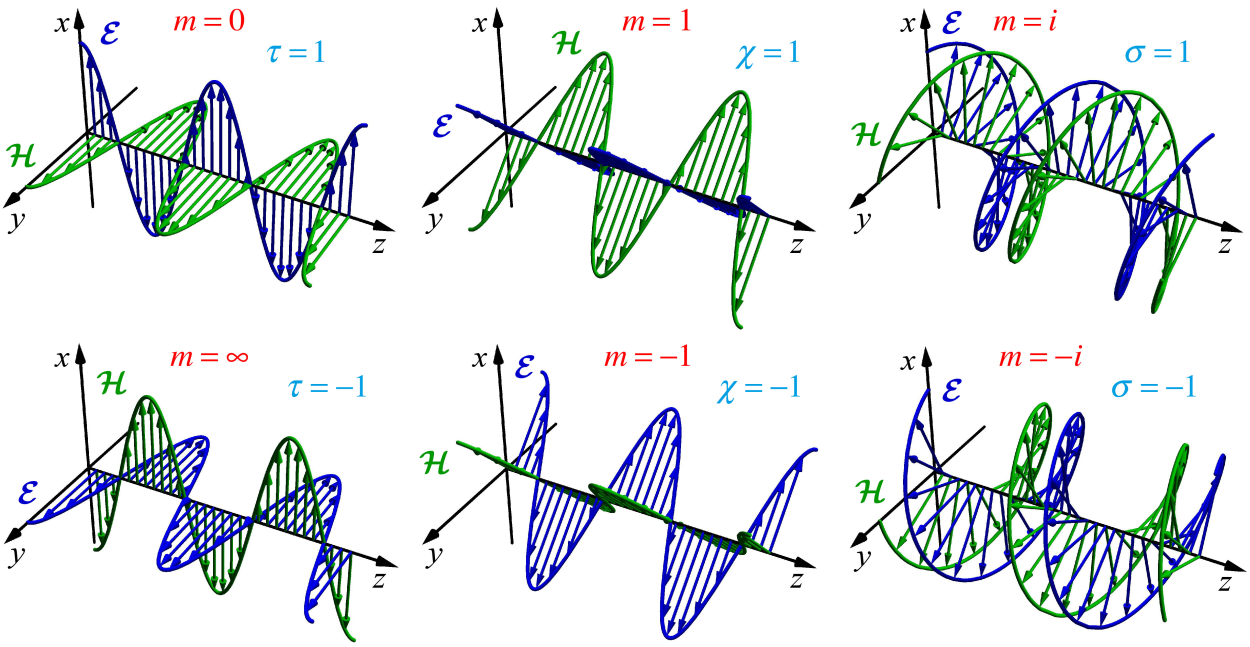

Supplementary Figure 1. Instantaneous distributions of the real electric and magnetic fields, $\boldsymbol{\mathcal{E}}(\mathbf{r},t)$ and $\boldsymbol{\mathcal{H}}(\mathbf{r},t)$, of the propagating plane wave (2.1). Six basic polarizations $\tau=\pm1$, $\chi=\pm1$, and $\sigma=\pm1$ are shown and marked with the corresponding values of the complex polarization parameter m.

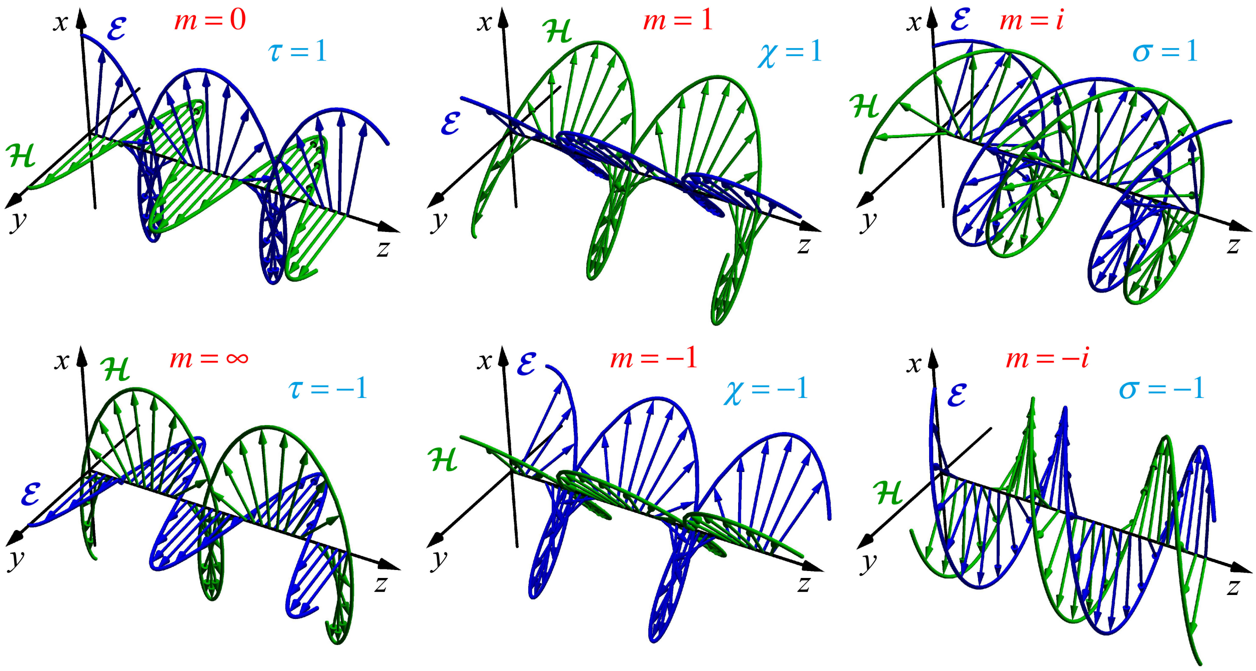

Supplementary Figure 2. Instantaneous distributions of the real electric and magnetic fields, $\boldsymbol{\mathcal{E}}(\mathbf{r},t)$ and $\boldsymbol{\mathcal{H}}(\mathbf{r},t)$, of the evanescent plane wave (2.4) and (2.5) [cf. the propagating plane wave in Supplementary Figure 1]. Six basic polarizations $\tau=\pm1$, $\chi=\pm1$, and $\sigma=\pm1$ are shown and marked with the corresponding values of the complex polarization parameter m.

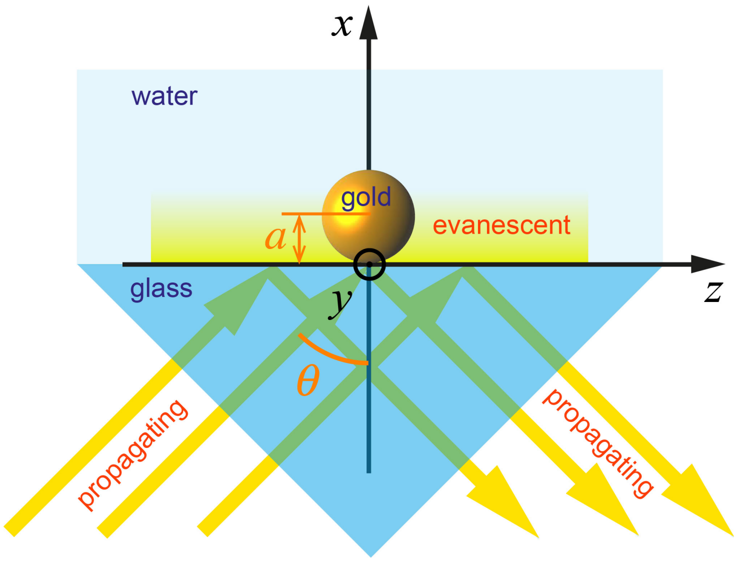

Supplementary Figure 3. Schematic of a proposed experiment observing the mechanical action of the evanescent field on a probe particle. The evanescent field is generated via the total internal reflection of the polarized light at the glass–water interface $x = 0$. A spherical gold particle of radius a is immersed in water on the surface of the glass. The radiation forces and torques cause linear and spinning motion of the particle, thereby, measuring the momentum and spin AM transfer from the evanescent field to the particle.

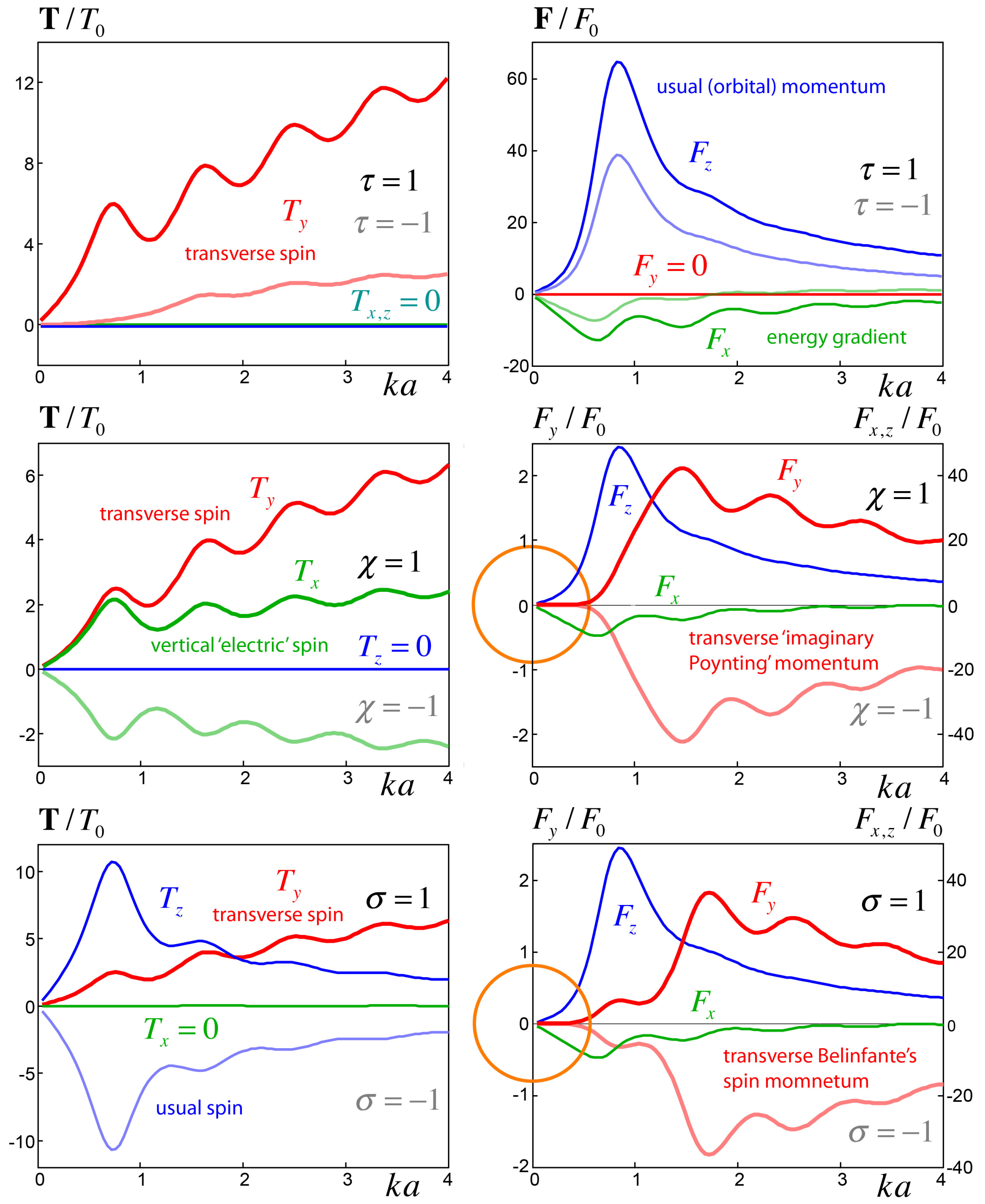

Supplementary Figure 4. Radiation forces and torques versus the particle size ka, numerically calculated for a gold Mie particle in the setup Supplementary Figure 3 with parameters (3.20). All components of the forces and torques are shown for six basic polarizations $\tau = \pm 1$, $\chi = \pm 1$, and $\sigma = \pm 1$ of the evanescent field. In addition to the known radiation-pressure longitudinal force, vertical gradient force, and longitudinal helicity-dependent torque, the following extraordinary forces and torques appear. The σ-independent torque T_y indicates the transverse helicity-independent spin in the evanescent wave. The vertical χ-dependent torque T_x reveals the presence of the vertical electric spin in the diagonally-polarized evanescent waves. Finally, the σ- and χ-dependent transverse forces F_y unveil the presence of the transverse Belinfante's spin momentum and 'imaginary' transverse Poynting vector (3.14). All the forces and torques and their correspondence to the field momenta and spins are summarized in Supplementary Table 1.

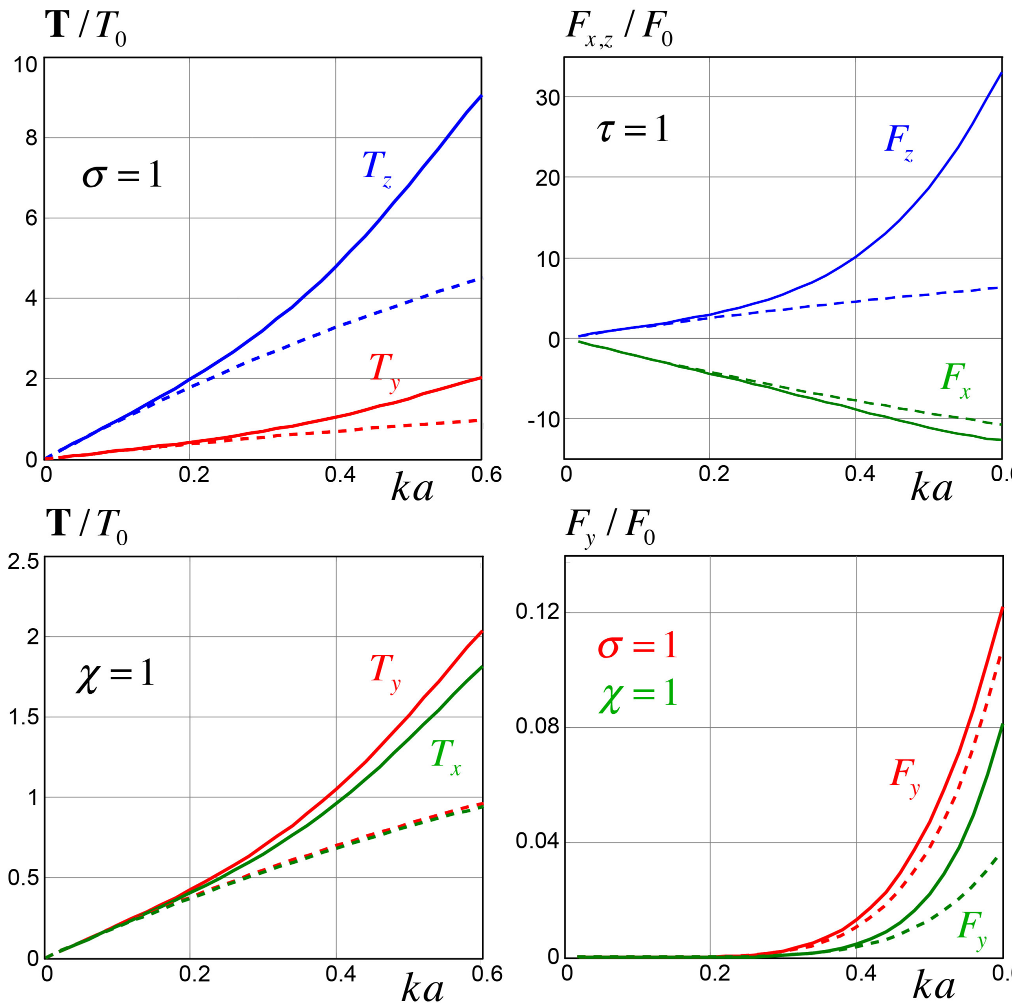

Supplementary Figure 5. Comparison between the numerical calculations (solid lines) and analytical dipole and dipole-dipole coupling approximations (dashed lines) for the radiation forces and torques on a small gold particle with $ka \ll 1$. Numerical calculations represent the exact Mie theory (the same as in Supplementary Figure 4), whereas the dipole and dipole-dipole approximations are described by Eqs. (3.6)–(3.15). One can see that the analytical equations describe the leading orders of the forces and torques in the Rayleigh-particle region $ka \ll 1$, but the exact forces and torques become significantly larger in the strong-coupling Mie region with $ka \sim 1$.

Field characteristics	**Action on a small particle**
Longitudinal canonical momentum $p_z^{\mathrm{O}} \propto k_z w$	Longitudinal τ -dependent electric-dipole radiation-pressure force $F_z \propto p_{\mathrm{e}z}^{\mathrm{O}} \propto -\left(1+\tau\dfrac{\kappa^2}{k_z^2}\right)p_z^{\mathrm{O}}$
Vertical imaginary canonical momentum $\operatorname{Im}\tilde{p}_x^{\mathrm{O}} \propto -\nabla_x w/2$	Vertical τ -dependent electric-dipole gradient force $F_x \propto -\operatorname{Im}\tilde{p}_{\mathrm{e}x}^{\mathrm{O}} \propto -\left(1+\tau\dfrac{\kappa^2}{k_z^2}\right)\operatorname{Im}\tilde{p}_x^{\mathrm{O}}$
Transverse helicity-dependent spin (Poynting) momentum $p_y^{\mathrm{S}} = p_y \propto \sigma\left(\kappa k/k_z\right)w$	Transverse σ -dependent part dipole-dipole force (3.12) $\tilde{F}_y \propto -p_y^{\mathrm{S}}$
Transverse imaginary Poynting momentum at diagonal polarizations $\operatorname{Im}\tilde{p}_y \propto -\chi\left(\kappa k/k_z\right)w$	Transverse χ -dependent part of the dipole-dipole force (3.12) $\tilde{F}_y \propto \operatorname{Im}\tilde{p}_y$
Longitudinal helicity-dependent spin $s_z \propto \sigma\left(k/k_z\right)w$	Longitudinal σ -dependent electric-dipole torque $T_z \propto s_{\mathrm{e}z} \propto s_z$
Transverse polarization-independent spin $s_y \propto \left(\kappa/k_z\right)w$	Transverse τ -dependent electric-dipole torque $T_y \propto s_{\mathrm{e}y} \propto (1+\tau)s_y$
Vertical electric and magnetic spins at diagonal polarizations $s_{\mathrm{e}x} = -s_{\mathrm{m}x} \propto \chi\left(\kappa k/k_z^2\right)w$	Vertical χ -dependent electric-dipole torque $T_x \propto s_{\mathrm{e}x}$

Supplementary Table 1. Four distinct momenta and three spins in a polarized evanescent wave versus their observable manifestations in the forces and torques on a small particle with $ka \ll 1$. One can trace the exact correspondence of these polarization-dependent forces and torques to the exact results (for $ka \sim 1$) shown in Supplementary Figure 4.

Supplementary Note 1. Harmonic Maxwell fields and their characteristics

We consider Maxwell equations for monochromatic electromagnetic fields in a uniform non-dispersive medium with permittivity ε and permeability μ:

$$\nabla \cdot \mathbf{H} = \nabla \cdot \mathbf{E} = 0\,, \quad -i\frac{\omega}{c}\varepsilon\,\mathbf{E} = \nabla \times \mathbf{H}\,, \quad -i\frac{\omega}{c}\mu\,\mathbf{H} = -\nabla \times \mathbf{E}\,. \tag{1.1}$$

Here ω is the frequency, c is the speed of light in vacuum, $\mathbf{E}(\mathbf{r})$ and $\mathbf{H}(\mathbf{r})$ are the complex electric and magnetic field amplitudes, whereas the real fields are given by $\boldsymbol{\mathcal{E}}(\mathbf{r},t) = \mathrm{Re}\left[\mathbf{E}(\mathbf{r})e^{-i\omega t}\right]$ and $\boldsymbol{\mathcal{H}}(\mathbf{r},t) = \mathrm{Re}\left[\mathbf{H}(\mathbf{r})e^{-i\omega t}\right]$, and throughout the paper we use Gaussian units.

The time-averaged energy density and Poynting momentum density of the monochromatic field are known to be [1]

$$w = \frac{g}{4}\left(\varepsilon|\mathbf{E}|^2 + \mu|\mathbf{H}|^2\right), \quad \mathbf{p} = \frac{g}{2c}\mathrm{Re}\left(\mathbf{E}^* \times \mathbf{H}\right), \tag{1.2}$$

where $g = 1/4\pi$ is the Gaussian-units coefficient. Although the Poynting vector $\mathbf{p}$ is usually considered as a meaningful momentum density of the field, in fact it represents a sum of two terms with quite different physical meanings. Using Maxwell equations (1.1), one can write it as $\mathbf{p} = \mathbf{p}^{\mathrm{O}} + \mathbf{p}^{\mathrm{S}}$ [2–5]:

$$\mathbf{p}^{\mathrm{O}} = \frac{g}{4\omega}\mathrm{Im}\left[\mu^{-1}\mathbf{E}^* \cdot (\boldsymbol{\nabla})\mathbf{E} + \varepsilon^{-1}\mathbf{H}^* \cdot (\boldsymbol{\nabla})\mathbf{H}\right], \tag{1.3}$$

$$\mathbf{p}^{\mathrm{S}} = \frac{g}{8\omega}\nabla \times \mathrm{Im}\left[\mu^{-1}\left(\mathbf{E}^* \times \mathbf{E}\right) + \varepsilon^{-1}\left(\mathbf{H}^* \times \mathbf{H}\right)\right]. \tag{1.4}$$

Here $\mathbf{p}^{\mathrm{O}}$ is the *canonical* or *orbital momentum density*, which is responsible for the energy transport and radiation pressure, whereas $\mathbf{p}^{\mathrm{S}}$ is the *spin momentum density*, which does not transport energy but generates the spin angular momentum (AM) of light [3,6–10]. (The spin momentum was introduced by Belinfante [7] in field theory for the explanation of spin of quantum particles and symmetrisation of the energy–momentum tensor.) It is the canonical momentum density $\mathbf{p}^{\mathrm{O}}$ that represents the observable momentum of light [2,3,11–15]; it characterizes the local wave vector of the field (multiplied by the intensity), which is mostly independent of the polarization. At the same time, the spin momentum density $\mathbf{p}^{\mathrm{S}}$ is a virtual solenoidal current, given by the curl of the *spin AM density*, $\mathbf{p}^{\mathrm{S}} = \boldsymbol{\nabla} \times \mathbf{s}/2$:

$$\mathbf{s} = \frac{g}{4\omega}\mathrm{Im}\left[\mu^{-1}\left(\mathbf{E}^* \times \mathbf{E}\right) + \varepsilon^{-1}\left(\mathbf{H}^* \times \mathbf{H}\right)\right]. \tag{1.5}$$

As it can be seen from their names, the orbital and spin momentum densities are responsible for the generation of the orbital and spin AM of light. Namely, the *orbital AM density* is defined in a straightforward way as $\mathbf{l} = \mathbf{r} \times \mathbf{p}^{\mathrm{O}}$, and this is an extrinsic origin-dependent quantity. At the same time, the spin AM density $\mathbf{s}$, Eq. (1.5), is intrinsic (origin-independent). Nonetheless, its integral value is determined by the circulation of the spin momentum (1.4): $\mathbf{S} = \int \mathbf{s}\,dV = \int \mathbf{r} \times \mathbf{p}^{\mathrm{S}} dV$, where integration by parts should be performed [3–10]. Thus, the spin momentum is similar to the boundary magnetization current or topological quantum-Hall-state current in solid-state systems, whereas the spin AM is analogous to the bulk magnetization in such systems.

In addition to the above dynamical characteristics of the field, there is one more fundamental quantity, namely, the *helicity density*. Recently, it caused considerable attention [5,16,17] in connection with the fundamental dual 'electric–magnetic' symmetry of Maxwell equations [18–20] and optical interaction with chiral particles [21–24]. The time-averaged helicity density of the monochromatic Maxwell field can be written as [5]

$$h = -\frac{g}{2\omega}\,\mathrm{Im}\left(\mathbf{E}^{*}\cdot\mathbf{H}\right). \tag{1.6}$$

The helicity characterizes the difference between the number of right-hand and left-hand circularly-polarized photons.

In free space, $\varepsilon = \mu = 1$, bilinear quantities (1.2)–(1.6) allow a convenient quantum-like representation in terms of the energy, momentum, and spin operators [2,5]. To show this, we introduce the local state vector of the field:

$$\vec{\psi}(\mathbf{r}) = \sqrt{\frac{g}{4\omega}}\begin{pmatrix} \mathbf{E}(\mathbf{r}) \\ \mathbf{H}(\mathbf{r}) \end{pmatrix}. \tag{1.7}$$

This is formally a vector in $\mathbb{C}^3 \otimes \mathbb{C}^2 \otimes \mathrm{L}^2$ space, where the 'dual' $\mathbb{C}^2$ space is associated with the electric and magnetic degrees of freedom. (Rigorously speaking, monochromatic fields are not square-integrable functions, but this does not affect our local analysis.) Using the state vector (1.7), the energy, canonical momentum, spin AM, and helicity densities can be written as 'local expectation values' of the corresponding operators:

$$w = \vec{\psi}^{\dagger}\cdot(\omega)\vec{\psi}\,, \tag{1.8}$$

$$\mathbf{p}^{\mathrm{O}} = \mathrm{Re}\left[\vec{\psi}^{\dagger}\cdot(\hat{\mathbf{p}})\vec{\psi}\right], \tag{1.9}$$

$$\mathbf{s} = \vec{\psi}^{\dagger}\cdot\left(\hat{\mathbf{S}}\right)\vec{\psi}\,, \tag{1.10}$$

$$h = \vec{\psi}^{\dagger}\cdot\left(-\hat{\sigma}_2\right)\vec{\psi} = \vec{\psi}^{\dagger}\cdot\left(\frac{\hat{\mathbf{p}}\cdot\hat{\mathbf{S}}}{p}\right)\vec{\psi}\,. \tag{1.11}$$

Here $\hat{\mathbf{p}} = -i\nabla$ is the canonical momentum operator in L^2 (we use units $\hbar = 1$). The spin operator $\hat{\mathbf{S}}$ in $\mathbb{C}^3$ is given by spin-1 matrices:

$$\hat{S}_x = -i\begin{pmatrix} 0 & 0 & 0 \\ 0 & 0 & 1 \\ 0 & -1 & 0 \end{pmatrix}, \quad \hat{S}_y = -i\begin{pmatrix} 0 & 0 & -1 \\ 0 & 0 & 0 \\ 1 & 0 & 0 \end{pmatrix}, \quad \hat{S}_z = -i\begin{pmatrix} 0 & 1 & 0 \\ -1 & 0 & 0 \\ 0 & 0 & 0 \end{pmatrix}, \tag{1.12}$$

(which act on the electric- and magnetic-field components as $\mathbf{E}^{*}\cdot\left(\hat{\mathbf{S}}\right)\mathbf{E} = \mathrm{Im}\left(\mathbf{E}^{*}\times\mathbf{E}\right)$ and $\mathbf{H}^{*}\cdot\left(\hat{\mathbf{S}}\right)\mathbf{H} = \mathrm{Im}\left(\mathbf{H}^{*}\times\mathbf{H}\right)$). Finally, the 'dual' operator in $\mathbb{C}^2$

$$\hat{\sigma}_2 = \begin{pmatrix} 0 & -i \\ i & 0 \end{pmatrix} \tag{1.13}$$

mixes the electric and magnetic subspaces. The eigenmodes of this operator, $\hat{\sigma}_2\vec{\psi} = \sigma\vec{\psi}$, with $\sigma = \pm 1$, are the fields with well-defined helicity: $\mathbf{H} = -i\sigma\mathbf{E}$. The last equality in Eq. (1.11) with $p = \omega/c$ represents a form of the last two Maxwell equations (1.1) in vacuum. This reveals the connection to the quantum-mechanical helicity as the spin projection onto the momentum direction. The Poynting momentum (1.2) can also be written in a quantum-like form, and it is characterized by a mixed energy–helicity–spin operator:

$$\mathbf{p} = \vec{\psi}^{\dagger} \cdot \left(-\omega \hat{\sigma}_2 \otimes \hat{\mathbf{S}}\right) \vec{\psi} \,. \tag{1.14}$$

Note that the 'local expectation values' of the quantum operators, Eqs. (1.8)–(1.11) and (1.14), can be interpreted in terms of *quantum weak measurements* [25–27]. For any operator $\hat{\mathbf{O}}$, the corresponding local density $\mathbf{O}(\mathbf{r})$ is proportional to the real part of the complex *non-normalized weak value* $\tilde{\mathbf{O}}(\mathbf{r})$ with the post-selection in the coordinate eigenstate [2,5,11,12]:

$$\tilde{\mathbf{O}}(\mathbf{r}) = \vec{\psi}^{\dagger}(\mathbf{r}) \cdot \left(\hat{\mathbf{O}}\right) \vec{\psi}(\mathbf{r}) = \langle \vec{\psi} | \mathbf{r} \rangle \langle \mathbf{r} | \hat{\mathbf{O}} | \vec{\psi} \rangle \,. \tag{1.15}$$

(As usual, 'bra' and 'ket' notations are used for the inner product in the L^2 Hilbert space.) In particular, the canonical momentum density (1.9) is the real part of the *complex* canonical momentum, or 'weak momentum':

$$\tilde{\mathbf{p}}^{\mathrm{O}}(\mathbf{r}) = \vec{\psi}^{\dagger}(\mathbf{r}) \cdot (\hat{\mathbf{p}}) \vec{\psi}(\mathbf{r}) = \langle \vec{\psi} | \mathbf{r} \rangle \langle \mathbf{r} | \hat{\mathbf{p}} | \vec{\psi} \rangle = \mathbf{p}^{\mathrm{O}}(\mathbf{r}) - i \frac{1}{2\omega} \nabla w(\mathbf{r}) \,. \tag{1.16}$$

Indeed, a recent remarkable experiment [12], which realized quantum weak measurements of the local momentum of photons, in fact measured $\mathbf{p}^{\mathrm{O}}(\mathbf{r})$ (with the imaginary part of the weak value (1.16) being also observable) [11].

Importantly, almost all meaningful dynamical characteristics (1.2)–(1.5) (except for the helicity (1.6)) naturally represent a sum of the electric- and magnetic-field contributions:

$$w = w_{\mathrm{e}} + w_{\mathrm{m}} \,, \quad \mathbf{p}^{\mathrm{O}} = \mathbf{p}_{\mathrm{e}}^{\mathrm{O}} + \mathbf{p}_{\mathrm{m}}^{\mathrm{O}} \,, \quad \mathbf{p}^{\mathrm{S}} = \mathbf{p}_{\mathrm{e}}^{\mathrm{S}} + \mathbf{p}_{\mathrm{m}}^{\mathrm{S}} \,, \quad \mathbf{s} = \mathbf{s}_{\mathrm{e}} + \mathbf{s}_{\mathrm{m}} \,. \tag{1.17}$$

The symmetry between the electric and magnetic contributions reflects the dual symmetry of the free-space Maxwell equations and fields. At the same time, matter is typically strongly dual-asymmetric (since it is built using electric but not magnetic charges), so that the electric and magnetic parts of the field characteristics can play very different roles in light–matter interactions (including measurement processes). The helicity (1.6) mixes electric and magnetic fields because it represents the generator of the dual transformations of Maxwell equations [5,16–20].

Supplementary Note 2. Application to evanescent wave fields

Evanescent wave fields. Consider first a polarized electromagnetic plane wave propagating along the z-axis in a medium with permittivity ε and permeability μ. The complex electric and magnetic fields can be written in Cartesian coordinates as

$$\mathbf{E}(\mathbf{r}) = \frac{A\sqrt{\mu}}{\sqrt{1+|m|^2}} \begin{pmatrix} 1 \\ m \\ 0 \end{pmatrix} \exp(ikz), \quad \mathbf{H}(\mathbf{r}) = \frac{A\sqrt{\varepsilon}}{\sqrt{1+|m|^2}} \begin{pmatrix} -m \\ 1 \\ 0 \end{pmatrix} \exp(ikz), \tag{2.1}$$

where A is the wave amplitude, $k = n\omega / c$ is the wavenumber, $n = \sqrt{\varepsilon\mu}$ is the refraction index of the medium, and the complex number m characterizes the polarization of the wave. Namely, $m = 0$ and $m = \infty$ correspond to the x (TM) and y (TE) linear polarizations; $m = \pm 1$ correspond to the diagonal and anti-diagonal linear polarizations at $\pm 45°$, and $m = \pm i$ describe the right- and left-hand circular polarizations. The degrees of the TE–TM, diagonal, and circular polarizations are described by the corresponding normalized Stokes parameters:

$$\tau = \frac{1-|m|^2}{1+|m|^2}, \quad \chi = \frac{2\,\mathrm{Re}\, m}{1+|m|^2}, \quad \sigma = \frac{2\,\mathrm{Im}\, m}{1+|m|^2}. \tag{2.2}$$

Here $\tau^2 + \chi^2 + \sigma^2 = 1$, and the third Stokes parameter σ determines the helicity (1.6) of the wave. Supplementary Figure 1 shows instantaneous distributions of the real electric and magnetic fields, $\boldsymbol{\mathcal{E}}(\mathbf{r},t)$ and $\boldsymbol{\mathcal{H}}(\mathbf{r},t)$, in the propagating wave (2.1) for six basic polarizations: $\tau = \pm 1$, $\chi = \pm 1$, and $\sigma = \pm 1$.

An evanescent plane wave propagating along the z-axis and decaying along the x-axis can be obtained from the plane wave (2.1) via an imaginary-angle rotation about the transverse y-axis [28]. Such rotation is described by the transformation matrix

$$\hat{R}(i\vartheta) = \begin{pmatrix} \cos(i\vartheta) & 0 & \sin(i\vartheta) \\ 0 & 1 & 0 \\ -\sin(i\vartheta) & 0 & \cos(i\vartheta) \end{pmatrix} = \begin{pmatrix} \cosh\vartheta & 0 & i\sinh\vartheta \\ 0 & 1 & 0 \\ -i\sinh\vartheta & 0 & \cosh\vartheta \end{pmatrix}. \tag{2.3}$$

Applying it to both vector components and spatial distribution of the fields (2.1), $\mathbf{E}(\mathbf{r}) \to \hat{R}(i\vartheta)\mathbf{E}\left[\hat{R}(-i\vartheta)\mathbf{r}\right]$, $\mathbf{H}(\mathbf{r}) \to \hat{R}(i\vartheta)\mathbf{H}\left[\hat{R}(-i\vartheta)\mathbf{r}\right]$, we derive the complex evanescent-wave fields [28]:

$$\mathbf{E}(\mathbf{r}) = \frac{A\sqrt{\mu}}{\sqrt{1+|m|^2}} \begin{pmatrix} 1 \\ mk/k_z \\ -i\kappa/k_z \end{pmatrix} \exp(ik_z z - \kappa x), \tag{2.4}$$

$$\mathbf{H}(\mathbf{r}) = \frac{A\sqrt{\varepsilon}}{\sqrt{1+|m|^2}} \begin{pmatrix} -m \\ k/k_z \\ im\kappa/k_z \end{pmatrix} \exp(ik_z z - \kappa x). \tag{2.5}$$

Here we introduced the propagation constant $k_z = k\cosh\vartheta > k$, the decay constant $\kappa = k\sinh\vartheta$, $k_z^2 - \kappa^2 = k^2$, and also renormalized the amplitude $A \to A/\cosh\vartheta$. One can readily verify that fields (2.4) and (2.5) satisfy Maxwell equations (1.1).

Supplementary Figure 2 shows the instantaneous distributions of the real electric and magnetic fields, $\boldsymbol{\mathcal{E}}(\mathbf{r},t)$ and $\boldsymbol{\mathcal{H}}(\mathbf{r},t)$, in the evanescent wave (2.4) and (2.5) for six basic polarizations: $\tau=\pm1$, $\chi=\pm1$, and $\sigma=\pm1$. The main difference, compared to the propagating wave (Supplementary Figure 1), is the presence of the *imaginary longitudinal* z*-components* in the complex fields (2.4) and (2.5). These components result in rotations of the electric and magnetic fields in the propagation (x,z) plane, which generate the transverse helicity-independent spin [see Eq. (2.14) below]. Furthermore, for diagonal polarizations $\chi=\pm1$, the electric and magnetic fields also rotate in the (y,z) plane, thereby generating the vertical electric and magnetic spins of the opposite signs [see Eq. (2.18) below].

The simplest way to generate the evanescent wave (2.4) and (2.5) in the $x>0$ half-space is to use the total internal reflection at the $x=0$ interface between a medium with parameters ε_1 and μ_1 (e.g., glass), and the medium with parameters ε and μ (e.g., water), such that $n_1=\sqrt{\varepsilon_1\mu_1}>n$. Let the incident plane wave of the type (2.1) with amplitude A_1, polarization m_1, and wave number $k_1=n_1\omega/c$ propagate in the glass at the angle $\theta>\theta_c\equiv\sin^{-1}(n/n_1)$ with respect to the x-axis, Supplementary Figure 3. Then, the transmitted wave in water ($x>0$) will be the evanescent wave (2.4) and (2.5) with the parameters given by

$$A=\frac{k_z}{k}\sqrt{\frac{\mu_1}{\mu}}TA_1\,,\quad k_z=k\frac{n_1}{n}\sin\theta\,,\quad \kappa=k\sqrt{\left(\frac{n_1}{n}\right)^2\sin^2\theta-1}\,,\quad m=\frac{T_\perp}{T_\parallel}m_1\,. \tag{2.6}$$

Here

$$T_\parallel=-\frac{2k\sqrt{\varepsilon_1/\mu_1}\cos\theta_1}{k\sqrt{\varepsilon/\mu}\cos\theta_1+i\kappa\sqrt{\varepsilon_1/\mu_1}}\,,\quad T_\perp=-\frac{2k\sqrt{\varepsilon_1/\mu_1}\cos\theta_1}{k\sqrt{\varepsilon_1/\mu_1}\cos\theta_1+i\kappa\sqrt{\varepsilon/\mu}} \tag{2.7}$$

are the Fresnel transmission coefficients for the TM and TE polarization components [1], whereas $T=\frac{\sqrt{|T_\parallel|^2+|m_1|^2|T_\perp|^2}}{\sqrt{1+|m_1|^2}}\exp\left[i\arg T_\parallel\right]$. In the case of near-critical incidence, $0<\theta-\theta_c\ll1$, the polarization of the transmitted evanescent wave can be approximated as $m\simeq\sqrt{\varepsilon\mu_1/\varepsilon_1\mu}\,m_1$, which shows a way for generating the evanescent wave of any desired polarization m by preparing the corresponding polarization m_1 of the incident wave.

Local characteristics of the evanescent field. Now we calculate the local dynamical characteristics of the evanescent wave (2.4) and (2.5). As a reference point, we first find the energy, momentum, spin, and helicity densities in the propagating plane wave (2.1). In this case, equations (1.2)–(1.6) result in

$$w=\gamma In^2\omega\,, \tag{2.8}$$

$$\mathbf{p}^{\mathrm{O}}=\mathbf{p}=\gamma Ik\,\hat{\mathbf{z}}\,,\quad \mathbf{p}^{\mathrm{S}}=\mathbf{0}\,, \tag{2.9}$$

$$\mathbf{s}=\gamma I\sigma\,\hat{\mathbf{z}}\,,\quad h=\gamma In\sigma\,, \tag{2.10}$$

where $\gamma=g/2\omega$, $I=|A|^2$ is the wave intensity, and $\hat{\mathbf{x}},\hat{\mathbf{y}},\hat{\mathbf{z}}$ denote the unit vectors of the corresponding axes. In vacuum ($n=1$), equations (2.8)–(2.10) yield

$$\mathbf{p}=\frac{w}{\omega}k\,\hat{\mathbf{z}}\,,\quad \mathbf{s}=\frac{w}{\omega}\sigma\,\hat{\mathbf{z}}\,,\quad h=\frac{w}{\omega}\sigma\,, \tag{2.11}$$

in agreement with the quantum-mechanical picture of photons.

Now, substituting fields (2.4) and (2.5) into equations (1.2)–(1.6), we derive the energy, momentum, spin, and helicity densities in the evanescent wave:

$$w = \gamma I n^2 \omega, \quad \mathbf{p} = \frac{w}{\omega n^2}\left(\frac{k^2}{k_z}\hat{\mathbf{z}} + \sigma \frac{\kappa k}{k_z}\hat{\mathbf{y}} \right), \tag{2.12}$$

$$\mathbf{p}^{\mathrm{O}} = \frac{w}{\omega n^2}\boxed{k_z \hat{\mathbf{z}}}, \quad \mathbf{p}^{\mathrm{S}} = \frac{w}{\omega n^2}\left(-\frac{\kappa^2}{k_z}\hat{\mathbf{z}} + \boxed{\sigma \frac{\kappa k}{k_z}\hat{\mathbf{y}}} \right), \tag{2.13}$$

$$\mathbf{s} = \frac{w}{\omega n^2}\left(\sigma \frac{k}{k_z}\hat{\mathbf{z}} + \boxed{\frac{\kappa}{k_z}\hat{\mathbf{y}}} \right), \quad h = \frac{w}{\omega n}\sigma, \tag{2.14}$$

where $I(x) = |A|^2 \exp(-2\kappa x)$ and $w(x)$ is now the inhomogeneous energy density in the wave. While the helicity and energy densities in Eqs. (2.12) and (2.14) have the same form as for the plane wave in Eqs. (2.8) and (2.10), the momentum and spin densities in Eqs. (2.12)–(2.14) reveal a number of extraordinary features discussed in the main text. As we mentioned, it is the orbital momentum $\mathbf{p}^{\mathrm{O}}$ that represents the observable momentum density in optical fields. In evanescent waves, it corresponds to the '*superluminal*' propagation $k_z > \omega / c$ [shown inside the blue box in Eqs. (2.13)], which can be detected via the anomalously large momentum transfer in both resonant [13] and non-resonant [11,29] light–matter interactions. The *spin* of evanescent waves acquires a *transverse polarization-independent component* $s_y \propto (\kappa / k_z) w$ [shown inside the red box in Eqs. (2.14)], which was predicted recently for surface plasmon-polaritons [30], and which arises from the rotation of the field vectors within the propagation (x,z) plane, see Supplementary Figure 2. Finally, evanescent waves possess *non-zero Belinfante's spin-momentum* density which originates from the presence of spin and inhomogeneous intensity $w(x)$ (see Fig. 2 in the main text). The transverse spin-momentum component determines the *helicity-dependent transverse Poynting momentum* $p_y = p_y^{\mathrm{S}} \propto \sigma(\kappa k / k_z) w$ [shown inside the orange box in Eqs. (2.13)], which was first noticed by Fedorov in 1955 [31]. However, in contrast to the Fedorov's and Imbert's conclusions, this 'virtual' momentum does not lead to energy transport and the standard radiation pressure. Nonetheless, as we show in this work, it can be detected via higher-order light–matter interactions owing to the absence of the transverse orbital momentum.

As we mentioned above, the interaction with real (usually, non-magnetic) particles is highly dual-asymmetric and mostly sensitive to the electric parts of the corresponding field characteristics. Electric and magnetic contributions to the energy, momentum, and spin densities are approximately equal in paraxial propagating fields [2]. However, this is not so for non-paraxial and evanescent fields. Therefore, we also determine separately the electric and magnetic parts (1.17) of the quantities (2.12)–(2.14). This results in

$$w_{\mathrm{e}} = \frac{1}{2}\left(1 + \tau \frac{\kappa^2}{k_z^2} \right) w, \quad w_{\mathrm{m}} = \frac{1}{2}\left(1 - \tau \frac{\kappa^2}{k_z^2} \right) w, \tag{2.15}$$

$$\mathbf{p}_{\mathrm{e}}^{\mathrm{O}} = \frac{w}{2\omega n^2}\boxed{\left(1 + \tau \frac{\kappa^2}{k_z^2} \right) k_z \hat{\mathbf{z}}}, \quad \mathbf{p}_{\mathrm{m}}^{\mathrm{O}} = \frac{w}{2\omega n^2}\left(1 - \tau \frac{\kappa^2}{k_z^2} \right) k_z \hat{\mathbf{z}}, \tag{2.16}$$

$$\mathbf{p}_{\mathrm{e}}^{\mathrm{S}} = \frac{w}{2\omega n^2}\left(-(1+\tau)\frac{\kappa^2}{k_z}\hat{\mathbf{z}} + \boxed{\sigma\frac{\kappa k}{k_z}\hat{\mathbf{y}}} \right), \quad \mathbf{p}_{m}^{\mathrm{S}} = \frac{w}{2\omega n^2}\left(-(1-\tau)\frac{\kappa^2}{k_z}\hat{\mathbf{z}} + \boxed{\sigma\frac{\kappa k}{k_z}\hat{\mathbf{y}}} \right), \tag{2.17}$$

$$\mathbf{s}_{\mathrm{e}} = \frac{w}{2\omega n^2}\left(\sigma\frac{k}{k_z}\hat{\mathbf{z}} + \boxed{(1+\tau)\frac{\kappa}{k_z}\hat{\mathbf{y}}} + \boxed{\chi\frac{\kappa k}{k_z^2}\hat{\mathbf{x}}} \right), \ \mathbf{s}_{\mathrm{m}} = \frac{w}{2\omega n^2}\left(\sigma\frac{k}{k_z}\hat{\mathbf{z}} + (1-\tau)\frac{\kappa}{k_z}\hat{\mathbf{y}} \boxed{-\chi\frac{\kappa k}{k_z^2}\hat{\mathbf{x}}} \right). \tag{2.18}$$

These equations reveal several remarkable features. First, the helicity σ-dependent terms in quantities (2.12)–(2.14) are equally divided into their electric and magnetic parts. Second, the helicity-independent terms of Eqs. (2.12)–(2.14) are asymmetrically divided into electric and magnetic parts depending on the first Stokes parameter τ, Eq. (2.2). This reflects the difference between the electric and magnetic properties of the TM and TE evanescent modes. Finally, the electric and magnetic parts of the spin AM density (2.18) unveil new *vertical* terms $s_{\mathrm{e}x} = -s_{\mathrm{m}x} \propto \chi\left(\kappa k / k_z^{w}\right) w$ [shown inside the green boxes in Eqs. (2.18)], which are proportional to the degree of the diagonal polarization χ (the second Stokes parameter). These terms originate from the rotation of the diagonally-polarized electric and magnetic field vectors in the (y,z) plane, see Supplementary Figure 2. Since the electric and magnetic vectors rotate in opposite senses in this plane, the electric and magnetic contributions cancel each other in the total spin density (2.14). However, interaction with an *electric*-dipole particle will reveal the non-zero electric part of this vertical χ-dependent spin density via the vertical radiation torque (see Supplementary Note 3 below).

Supplementary Note 3. Mechanical action of the fields on small particles

Analytical calculations for dipole interactions. A straightforward way to measure the local dynamical characteristic of an optical field (momentum, spin, etc.) is to measure the mechanical action of the field on small probe particles. Therefore, we examine optical forces and torques that appear upon interaction with a small spherical particle. Analytical results can be obtained in the Rayleigh dipole-interaction approximation, when the particle radius a is much smaller than the wavelength: $ka \ll 1$.

A neutral particle in a monochromatic field can be characterized by the complex electric and magnetic dipole moments, $\mathbf{d}_{\mathrm{e}}$ and $\mathbf{d}_{\mathrm{m}}$, induced by the field:

$$\mathbf{d}_{\mathrm{e}} = \alpha_{\mathrm{e}} \mathbf{E}, \quad \mathbf{d}_{\mathrm{m}} = \alpha_{\mathrm{m}} \mathbf{H}, \tag{3.1}$$

where α_{e} and α_{m} are the complex electric and magnetic polarizabilities. Using the real dipole moments, $\boldsymbol{\mathfrak{d}}_{\mathrm{e}}(\mathbf{r},t) = \mathrm{Re}\left[\mathbf{d}_{\mathrm{e}}(\mathbf{r}) e^{-i\omega t}\right]$ and $\boldsymbol{\mathfrak{d}}_{\mathrm{m}}(\mathbf{r},t) = \mathrm{Re}\left[\mathbf{d}_{\mathrm{m}}(\mathbf{r}) e^{-i\omega t}\right]$, of the particle, the time-averaged optical force $\mathbf{F}$ and torque $\mathbf{T}$ are given by [1,32,33]

$$\mathbf{F} = \left\langle (\boldsymbol{\mathfrak{d}}_{\mathrm{e}} \cdot \nabla) \boldsymbol{\mathcal{E}} + (\boldsymbol{\mathfrak{d}}_{\mathrm{m}} \cdot \nabla) \boldsymbol{\mathcal{H}} + \frac{1}{c} \dot{\boldsymbol{\mathfrak{d}}}_{\mathrm{e}} \times \boldsymbol{\mathcal{B}} - \frac{1}{c} \dot{\boldsymbol{\mathfrak{d}}}_{\mathrm{m}} \times \boldsymbol{\mathcal{D}} \right\rangle, \tag{3.2}$$

$$\mathbf{T} = \left\langle \boldsymbol{\mathfrak{d}}_{\mathrm{e}} \times \boldsymbol{\mathcal{E}} + \boldsymbol{\mathfrak{d}}_{\mathrm{m}} \times \boldsymbol{\mathcal{H}} \right\rangle, \tag{3.3}$$

where $\boldsymbol{\mathcal{B}} = \mu \boldsymbol{\mathcal{H}}$, $\boldsymbol{\mathcal{D}} = \varepsilon \boldsymbol{\mathcal{E}}$, and $\langle ... \rangle$ stands for time averaging. Using Maxwell equations (1.1), we derive expression for the optical force and torque in terms of complex fields and dipole moments:

$$\mathbf{F} = \frac{1}{2} \mathrm{Re}\left[\mathbf{d}_{\mathrm{e}}^{*} \cdot (\nabla) \mathbf{E} + \mathbf{d}_{\mathrm{m}}^{*} \cdot (\nabla) \mathbf{H}\right]. \tag{3.4}$$

$$\mathbf{T} = \frac{1}{2} \mathrm{Re}\left[\mathbf{d}_{\mathrm{e}}^{*} \times \mathbf{E} + \mathbf{d}_{\mathrm{m}}^{*} \times \mathbf{H}\right]. \tag{3.5}$$

Substituting Eq. (3.1) into Eqs. (3.4) and (3.5) and using the expressions (1.2), (1.3), (1.5), and (1.17), we obtain the optical force and torque in terms of the dynamical characteristics of the field [2,15,34–37]:

$$\mathbf{F} = \frac{\gamma^{-1}}{2\omega n^2} \left[\mu \mathrm{Re}(\alpha_{\mathrm{e}}) \nabla w_{\mathrm{e}} + \varepsilon \mathrm{Re}(\alpha_{\mathrm{m}}) \nabla w_{\mathrm{m}}\right] + \gamma^{-1} \left[\mu \mathrm{Im}(\alpha_{\mathrm{e}}) \mathbf{p}_{\mathrm{e}}^{\mathrm{O}} + \varepsilon \mathrm{Im}(\alpha_{\mathrm{m}}) \mathbf{p}_{\mathrm{m}}^{\mathrm{O}}\right], \tag{3.6}$$

$$\mathbf{T} = \gamma^{-1} \left[\mu \mathrm{Im}(\alpha_{\mathrm{e}}) \mathbf{s}_{\mathrm{e}} + \varepsilon \mathrm{Im}(\alpha_{\mathrm{m}}) \mathbf{s}_{\mathrm{m}}\right]. \tag{3.7}$$

The first term in square brackets in Eq. (3.6) describes the *gradient force*, while the second term is the scattering force responsible for *optical pressure*. Thus, the optical pressure is determined by the *orbital momentum density* (1.3) rather than the Poynting vector. For an 'ideal' dual-symmetric particle with $\alpha_{\mathrm{e}} = \alpha_{\mathrm{m}} = \alpha$ in free space, the gradient and scattering radiation forces 'measure' the imaginary and real parts of the *complex* canonical momentum (1.16) of photons [11]:

$$\mathbf{F} = \gamma^{-1} \left[-\mathrm{Re}(\alpha) \mathrm{Im}\, \tilde{\mathbf{p}}^{\mathrm{O}} + \mathrm{Im}(\alpha) \mathrm{Re}\, \tilde{\mathbf{p}}^{\mathrm{O}}\right]. \tag{3.8}$$

Furthermore, the torque (3.7) is proportional to the corresponding electric and magnetic parts of the *spin* density (1.5). The optical pressure and torque are proportional to the imaginary parts of the particle polarizabilities (which are related to the absorption) and to the frequency ω (in the factor γ^{-1}). Therefore, this force and torque can be interpreted as the momentum and spin AM transfer rates, from the field to the particle. Moreover, taking into account that the lowest order (in ka) term of the polarizability is proportional to a^3 (i.e., to the particle's volume), one can conclude that this momentum and spin AM transfer 'measures' meaningful momentum and spin AM densities $\mathbf{p}^{\mathrm{O}} \propto \omega^{-1}\mathbf{F}_{\mathrm{scat}} / a^3$ and $\mathbf{s} \propto \omega^{-1}\mathbf{T} / a^3$. Of course, the particle would 'measure' the proper dual-symmetric field characteristics only in the 'ideal' case of equal electric and magnetic polarizabilities. In practice, they differ significantly (due to the dual asymmetry of matter), and hence the electric and magnetic parts of the field properties are obtained with different efficiencies.

For a spherical particle made of a material with complex permittivity ε_{p} and permeability μ_{p}, the electric and magnetic polarizabilities can be obtained from the Mie scattering coefficients. In the leading orders in ka, this results in [38–40]

$$\alpha_{\mathrm{e}} = \frac{\varepsilon}{k^3}\left\{ \frac{\varepsilon_{\mathrm{p}} - \varepsilon}{\varepsilon_{\mathrm{p}} + 2\varepsilon}(ka)^3 + \frac{3}{10}\frac{\varepsilon_{\mathrm{p}}^2 + \varepsilon_{\mathrm{p}}\varepsilon\left[\left(\varepsilon_{\mathrm{p}}\mu_{\mathrm{p}} / \varepsilon\mu\right) - 6\right] + 4\varepsilon^2}{\left(\varepsilon_{\mathrm{p}} + 2\varepsilon\right)^2}(ka)^5 \right\}, \tag{3.9}$$

$$\alpha_{m} = \frac{\mu}{k^3}\left\{ \frac{\mu_{\mathrm{p}} - \mu}{\mu_{\mathrm{p}} + 2\mu}(ka)^3 + \frac{3}{10}\frac{\mu_{\mathrm{p}}^2 + \mu_{\mathrm{p}}\mu\left[\left(\varepsilon_{\mathrm{p}}\mu_{\mathrm{p}} / \varepsilon\mu\right) - 6\right] + 4\mu^2}{\left(\mu_{\mathrm{p}} + 2\mu\right)^2}(ka)^5 \right\}. \tag{3.10}$$

Usually both the particle and the surrounding medium are *non-magnetic*: $\mu_{\mathrm{p}} = \mu = 1$. This results in the following leading-order polarizabilities (3.9) and (3.10):

$$\alpha_{\mathrm{e}} \simeq \frac{1}{k^3}\frac{\varepsilon\left(\varepsilon_{\mathrm{p}} - \varepsilon\right)}{\varepsilon_{\mathrm{p}} + 2\varepsilon}(ka)^3, \quad \alpha_{\mathrm{m}} = \frac{1}{k^3}\frac{\left(\varepsilon_{\mathrm{p}} - \varepsilon\right)}{30\,\varepsilon}(ka)^5. \tag{3.11}$$

In this case, $|\alpha_{\mathrm{m}}| \ll |\alpha_{\mathrm{e}}|$, and in most cases one can consider only electric parts of the forces and torques (3.6) and (3.7), which 'measure' the *electric* parts of the corresponding field characteristics.

Applying the above calculations to the evanescent wave (2.4) and (2.5) with characteristics (2.15)–(2.18), brings about the following results. The longitudinal optical-pressure force will 'measure' the corresponding electric part of the canonical momentum $p_{\mathrm{e}z}^{\mathrm{O}}$ [shown inside the blue box in Eq. (2.16)]. The vertical gradient electric-dipole force will indicate the x-gradient of the electric energy density $w_{\mathrm{e}}(x)$ [i.e., the 'imaginary' part $\mathrm{Im}\,\tilde{p}_{\mathrm{e}x}^{\mathrm{O}}$ of the corresponding complex momentum, see Eqs. (1.16) and (3.8)]. The longitudinal σ-dependent torque will appear due to the usual helicity-dependent z-component of the spin $s_{\mathrm{e}z}$. The transverse σ-independent torque will unveil the helicity-independent y-component of the spin $s_{\mathrm{e}y}$ [shown inside the red box in Eq. (2.18)]. Finally, the particle will also experience the χ-dependent vertical torque due to the presence of the non-zero x-component of the electric spin $s_{\mathrm{e}x}$ [shown inside the green box in Eq. (2.18)]. All of these results can be clearly seen in the numerical simulations in Supplementary Figures 4 and 5 and are summarized in Supplementary Table 1.

So far we mostly considered the dipole interactions proportional to the particle volume a^3. These interactions are sensitive to the field energy, canonical momentum, and spin densities. At the same time, they do *not* involve *Belinfante's spin momentum* (1.4), which confirms its 'virtual' character. Nonetheless, below we show that the spin momentum, as well as other remarkable quantities, appears in higher-order terms of light–matter interactions. The next-order interaction is the dipole-dipole coupling between the induced electric and magnetic moments. Taking it into account, one can calculate the corresponding force, which is the mixed electric-magnetic force described in [39,40]:

$$\tilde{\mathbf{F}} = \frac{\gamma^{-1}}{3} k^3 \left[-\mathrm{Re}\left(\alpha_{\mathrm{e}} \alpha_{\mathrm{m}}^*\right) \mathrm{Re}\, \tilde{\mathbf{p}} + \mathrm{Im}\left(\alpha_{\mathrm{e}} \alpha_{\mathrm{m}}^*\right) \mathrm{Im}\, \tilde{\mathbf{p}} \right]. \tag{3.12}$$

Here we introduced the *complex Poynting momentum* $\tilde{\mathbf{p}}$ defined as [1]

$$\tilde{\mathbf{p}} = \frac{g}{2c}\left(\mathbf{E}^* \times \mathbf{H}\right), \quad \mathrm{Re}\, \tilde{\mathbf{p}} = \mathbf{p} = \mathbf{p}^{\mathrm{O}} + \mathbf{p}^{\mathrm{S}}, \quad \mathrm{Im}\, \tilde{\mathbf{p}} = \frac{g}{2c} \mathrm{Im}\left(\mathbf{E}^* \times \mathbf{H}\right). \tag{3.13}$$

Thus, the two terms in the dipole-dipole force (3.12) are proportional to the total Poynting momentum $\mathbf{p}$ (including both the orbital and spin parts) and 'imaginary' Poynting momentum $\mathrm{Im}\, \tilde{\mathbf{p}}$, characterizing an alternating flow of the so-called 'stored energy' [1].

Usually, the spin momentum is accompanied by a non-zero orbital momentum, and the dipole-dipole force (3.12) is negligible compared to the main dipole force (3.6). However, evanescent waves offer a *unique* opportunity to study the *pure* spin transverse momentum $p_y^{\mathrm{S}} = p_y \propto \sigma\left(\kappa k / k_z\right) w$ [shown inside the orange box in Eq. (2.13)], without any orbital component. In this case, the transverse dipole force vanishes, and the transverse spin momentum induces *the transverse* σ*-dependent dipole-dipole force* (3.12) . This offers the *first direct observation* of the fundamental field-theory quantity, introduced in 1939 by Belinfante [7], remarked in optics in 1955 by Fedorov [31], and which was previously considered as 'virtual'. To determine the action of the second term in the force (3.12), we calculate the 'imaginary' Poynting momentum in the evanescent wave (2.4) and (2.5). This yields

$$\mathrm{Im}\, \tilde{\mathbf{p}} = \frac{w}{\omega n^2} \left(-\tau \frac{\kappa k^2}{k_z^2} \hat{\mathbf{x}} - \boxed{\chi \frac{\kappa k}{k_z} \hat{\mathbf{y}}} \right). \tag{3.14}$$

The force (3.12) from the vertical x-component $\mathrm{Im}\, \tilde{p}_x$ will be negligible as compared with the dipole gradient force (3.6). At the same time, the transverse component of the 'imaginary' Poynting momentum $\mathrm{Im}\, \tilde{p}_y$ [shown inside the magenta box in Eq. (3.14)] will result in a finite *transverse* χ*-dependent dipole-dipole force* (3.12) in the diagonally-polarized fields. This force represents a quite intriguing result, namely, a finite optical force at *zero* transverse momentum and intensity gradient: $p_y = p_y^{\mathrm{O}} = p_y^{\mathrm{S}} = 0$ at $\chi = \pm 1$. The presence of the transverse polarization-dependent dipole-dipole forces (3.12) can be clearly seen in the numerical simulations in Supplementary Figures 4 and 5, and these results are summarized in Supplementary Table 1.

For non-magnetic particle with polarizabilities (3.11), the coefficients in the dipole-dipole forces (3.12) take the form:

$$\mathrm{Re}\left(\alpha_{\mathrm{e}} \alpha_{\mathrm{m}}^*\right) \simeq \frac{1}{30 k^6} \left| \frac{\varepsilon_{\mathrm{p}} - \varepsilon}{\varepsilon_{\mathrm{p}} + 2\varepsilon} \right|^2 \left(\mathrm{Re}\, \varepsilon_{\mathrm{p}} + 2\right) (ka)^8, \quad \mathrm{Im}\left(\alpha_{\mathrm{e}} \alpha_{\mathrm{m}}^*\right) \simeq -\frac{1}{30 k^6} \left| \frac{\varepsilon_{\mathrm{p}} - \varepsilon}{\varepsilon_{\mathrm{p}} + 2\varepsilon} \right|^2 \mathrm{Im}\, \varepsilon_{\mathrm{p}} (ka)^8. \tag{3.15}$$

Exact numerical calculations for Mie particles in evanescent fields. Up to now, we described optical forces and torques in the case of small Rayleigh particles, $ka \ll 1$, which allows analytical evaluations and a clear physical interpretation. However, the forces and torques are small in this limit and rapidly grow with ka. Therefore, experimental measurements would be more appropriate and feasible when employing Mie particles of moderate size $ka \sim 1$. In this case, the optical forces and torques can be calculated numerically using the exact Mie scattering solutions. Recently, we generalized the Mie scattering solutions for the case of the incident evanescent fields (2.4) and (2.5) [28]. This method is based on the complex-angle rotation (2.3) of the known Mie solutions, and it was approved by comparison with other exact numerical methods. Using the modified Mie procedure of [28], the electric and magnetic fields scattered by a spherical Mie particle in the evanescent wave can be calculated from the evanescent electric field (2.4):

$$\mathbf{E}'(\mathbf{r}) = \hat{\mathrm{M}}_{\mathrm{E}}(\mathbf{r})\mathbf{E}, \quad \mathbf{H}'(\mathbf{r}) = \hat{\mathrm{M}}_{\mathrm{H}}(\mathbf{r})\mathbf{E}, \tag{3.16}$$

where the matrices $\hat{\mathrm{M}}_{\mathrm{E,H}}(\mathbf{r})$ include the standard Mie scattering operators and complex-angle rotational operators (2.3). The total electromagnetic field is then given by the sum of the incident and scattered fields:

$$\mathbf{E}^{\mathrm{tot}} = \mathbf{E} + \mathbf{E}', \quad \mathbf{H}^{\mathrm{tot}} = \mathbf{H} + \mathbf{H}'. \tag{3.17}$$

Once the total field is known, the radiation force can be calculated using the momentum-flux (stress) and the AM-flux tensors, $\hat{\mathcal{T}} = \{\mathcal{T}_{ij}\}$ and $\hat{\mathcal{M}} = \{\mathcal{M}_{ij}\}$:

$$\mathcal{T}_{ij} = \frac{g}{2}\mathrm{Re}\left[\varepsilon E_i^{\mathrm{tot}*} E_j^{\mathrm{tot}} + \mu H_i^{\mathrm{tot}*} H_j^{\mathrm{tot}} - \frac{1}{2}\delta_{ij}\left(\varepsilon\left|\mathbf{E}^{\mathrm{tot}}\right|^2 + \mu\left|\mathbf{H}^{\mathrm{tot}}\right|^2\right)\right], \quad \mathcal{M}_{ij} = \epsilon_{jkl} x_k \mathcal{T}_{li}, \tag{3.18}$$

where ϵ_{ijk} is the Levi-Civita symbol, indices take on values x, y, z, and summation over repeating indices is assumed. Integrating the momentum and AM fluxes (3.18) over any surface Σ enclosing the particle (e.g., a sphere $\Sigma = \{r = R\}$, $R > a$), we obtain the optical force and torque on the particle:

$$\mathbf{F} = \oint_{\Sigma} \hat{\mathcal{T}}\,\mathbf{n}\, d\Sigma, \quad \mathbf{T} = \oint_{\Sigma} \hat{\mathcal{M}}\,\mathbf{n}\, d\Sigma, \tag{3.19}$$

where $d\Sigma = R^2 \sin\theta d\theta d\phi$ is the elementary surface area in spherical coordinates $r\cos\theta = z$, $r\sin\theta\cos\phi = x$, $r\sin\theta\sin\phi = y$, and $\mathbf{n} = (\sin\theta\cos\phi, \sin\theta\sin\phi, \cos\theta)^T$ is the unit vector of the outer normal of the surface Σ. Note that, as in most other works, in this method we do not account for multiple reflections from the surface limiting the evanescent field. More accurate treatments show that the influence of these reflections is negligible in a wide range of parameters: e.g., in calculations of the force components parallel to the surface, and for particle sizes of the order of the wavelength and not exhibiting resonances [28,29,41–44].

Now, we perform numerical simulations based on the above calculation scheme. For this modelling, we choose the setup and parameters typical for many experiments on evanescent-wave manipulation of Mie particles [45–49]. Namely, we consider the evanescent wave generated via total internal reflection at the interface $x = 0$ between glass (usually, heavy flint glass or sapphire) and water, Supplementary Figure 3. A gold spherical particle is placed in water on the surface of glass (to reduce the friction between the particle and glass), so that its centre is located at $x_{\mathrm{p}} = a$. The generation of the evanescent wave in the total reflection is described by Eqs. (2.6) and (2.7), and all materials are non-magnetic, $\mu_1 = \mu = \mu_{\mathrm{p}} = 1$. The other parameters are:

$$\varepsilon_1 = 3.06, \quad \varepsilon = 1.77, \quad \varepsilon_{\mathrm{p}} = -12.2 + 3i, \quad \theta = 51^\circ \ (\theta_{\mathrm{c}} = 49.5^\circ), \quad \kappa / k = 0.21, \tag{3.20}$$

and the wavelength in vacuum is assumed to be $\lambda_0 = 2\pi c / \omega = 650\,\mathrm{nm}$. Using these parameters, we calculate all components of the radiation force and torque on the particle for six basic polarizations of the evanescent field: $\tau = \pm 1$, $\chi = \pm 1$, and $\sigma = \pm 1$. The results, as functions of the particle size ka, are presented in Supplementary Figure 4, where the forces and torques are normalized by the following quantities:

$$F_0 = \frac{a^2}{4\pi}\left|A_1\right|^2, \quad T_0 = \frac{F_0}{k}, \tag{3.21}$$

Here the normalization factor involves the square of the particle size to improve the visibility of the data for both small- and moderate-size particle (as it was also used in [28,41]), and we recall that $|A_1|^2$ is the intensity of the incident plane wave in the glass.

Supplementary Figure 4 shows the presence of all forces and torques (3.6), (3.7), (3.12), which quantify the four distinct momenta and three distinct spins in characteristics (2.12)–(2.18) and (3.14) of the evanescent field. This correspondence is summarized in Supplementary Table 1. Most importantly, the σ-independent torque T_y indicates the transverse helicity-independent spin in the evanescent wave [shown inside the red box in Eqs. (2.14) and (2.18)]. Next, the vertical χ-dependent torque T_x reveals the presence of the vertical electric spin in the diagonally-polarized evanescent waves [shown inside the green box in Eq. (2.18)]. Finally, the σ- and χ-dependent transverse forces F_y unveil the presence of the helicity-dependent transverse spin momentum [shown inside the orange boxes in Eqs. (2.13) and (2.17)] and 'imaginary' transverse Poynting vector [shown inside the magenta box in Eqs. (3.14)]. Note that these transverse forces are one order of magnitude weaker than typical radiation forces, F_z and F_x, and they vanish in the Rayleigh-particle limit $ka \ll 1$. Although the analytical expressions for the forces and torques, (3.6), (3.7), (3.12), are derived in the $ka \ll 1$ approximation, the exact forces and torques in Supplementary Figure 4 show the same polarization dependence and quantitative picture for larger particles with $ka \sim 1$.

In Supplementary Figure 5 we compare the exact numerical calculations of Supplementary Figure 4 with approximate analytical expression for forces and torques on a Rayleigh particle with $ka \ll 1$, Eqs. (3.6)–(3.15). One can see that the dipole and dipole-dipole weak-coupling approximations describe the leading orders of the forces and torques in the Rayleigh $ka \ll 1$ limit, but the exact forces and torques usually become larger in the strong-coupling Mie region with $ka \sim 1$.

Thus, we have shown that evanescent electromagnetic waves can carry *four* distinct momenta and *three* distinct spin angular momenta. This is in sharp contrast with the single momentum and single spin for a propagating plane wave (photons). Each of these momenta and spins has a clear physical meaning and result in a corresponding *directly-observable* force or torque on a probe Mie particle, as shown in Supplementary Figure 4. The field characteristics are given in Eqs. (2.12)–(2.18) and (3.14), whereas the forces and torques are described by Eqs. (3.6), (3.7), (3.11), and (3.12) in the $ka \ll 1$ approximation. These results are summarized in Supplementary Table 1, which shows excellent agreement with the exact numerical simulations in Supplementary Figure 4.

Supplementary References

1. Jackson, J.D. *Classical Electrodynamics* 3rd ed. (Wiley, 1999).
2. Berry, M.V. Optical currents. *J. Opt. A: Pure Appl. Opt.* **11**, 094001 (2009).
3. Bekshaev, A., Bliokh, K.Y. & Soskin, M. Internal flows and energy circulation in light beams. *J. Opt.* **13**, 053001 (2011).
4. Bliokh, K.Y. & Nori, F. Transverse spin of a surface polariton. *Phys. Rev. A* **85**, 061801(R) (2012).
5. Bliokh, K.Y., Bekshaev, A.Y. & Nori, F. Dual electromagnetism: helicity, spin, momentum, and angular momentum. *New J. Phys.* **15**, 033026 (2013).
6. Soper, D.E. *Classical Field Theory* (Wiley, 1976).
7. Belinfante, F.J. On the current and the density of the electric charge, the energy, the linear momentum and the angular momentum of arbitrary fields. *Physica* **7**, 449–474 (1940).
8. Ohanian, H.C. What is spin? *Am. J. Phys.* **54**, 500–505 (1986).
9. Mita, K. Virtual probability current associated with the spin. *Am. J. Phys.* **68**, 259–264 (2000).
10. Witting, C. Photon and electron spins. *J. Phys. Chem. A* **113**, 15320–15327 (2009).
11. Bliokh, K.Y., Bekshaev, A.Y., Kofman, A.G. & Nori, F. Photon trajectories, anomalous velocities, and weak measurements: a classical interpretation. *New J. Phys.* **15**, 073022 (2013).
12. Kocsis, S., Braverman, B., Ravets, S., Stevens, M.J., Mirin, R.P., Shalm, L.K. & Steinberg, A.M. Observing the average trajectories of single photons in a two-slit interferometer. *Science* **332**, 1170–1173 (2011).
13. Huard, S. & Imbert, C. Measurement of exchanged momentum during interaction between surface-wave and moving atom. *Opt. Commun.* **24**, 185–189 (1978).
14. Barnett, S.M. & Berry, M.V. Superweak momentum transfer near optical vortices. *J. Opt.* **15**, 125701 (2013).
15. Liberal, I., Ederra, I., Gonzalo, R. & Ziolkowski, R.W. Electromagnetic force density in electrically and magnetically polarizable media. *Phys. Rev. A* **88**, 053808 (2013).
16. Fernandez-Corbaton, I., Zambrana-Puyalto, X. & Molina-Terriza, G. Helicity and angular momentum: a symmetry-based framework for the study of light–matter interactions. *Phys. Rev. A* **86**, 042103 (2012).
17. Cameron, R.P., Barnett, S.M. & Yao, A.M. Optical helicity, optical spin, and related quantities in electromagnetic theory. *New J. Phys.* **14**, 053050 (2012).
18. Calcin, M.G. An invariance property of the free electromagnetic field. *Am. J. Phys.* **33**, 958–960 (1965).
19. D. Zwanziger, Quantum field theory of particles with both electric and magnetic charges, *Phys. Rev. D* **176**, 1489 (1968).
20. S. Deser and C. Teitelboim, Duality transformations of Abelian and non-Abelian gauge fields, *Phys. Rev. D* **13**, 1592 (1976).
21. Y. Tang and A.E. Cohen, Optical chirality and its interaction with matter, *Phys. Rev. Lett.* **104**, 163901 (2010).
22. Y. Tang and A.E. Cohen, Enhanced enantioselectivity in excitation of chiral molecules by superchiral light, *Science* **332**, 333 (2011).
23. K.Y. Bliokh and F. Nori, Characterizing optical chirality, *Phys. Rev. A* **83**, 021803(R) (2011).
24. H. Rhee, J.S. Choi, D.J. Starling, J.C. Howell, and M. Cho, Amplification of chiroptical spectroscopy, optical enantioselectivity, and weak value measurement, *Chem. Sci.* **4**, 4107–4114 (2013).
25. Y. Aharonov, D. Z. Albert, and L. Vaidman, How the result of a measurement of a component of the spin of a spin-1/2 particle can turn out to be 100, *Phys. Rev. Lett.* **60**, 1351 (1988);

26. A.G. Kofman, S. Ashhab, and F. Nori, Nonperturbative theory of weak pre- and post-selected measurements, *Phys. Rep.* **520**, 43 (2012).
27. J. Dressel, M. Malik, F.M. Miatto, A.N. Jordan, and R.W. Boyd, Understanding quantum weak values: basics and applications, Preprint at http://arxiv.org/abs/1305.7154 (2013).
28. Bekshaev, A.Y., Bliokh, K.Y. & Nori, F. Mie scattering and optical forces from evanescent fields: a complex-angle approach. *Opt. Express* **21**, 7082–7095 (2013).
29. Nieto-Vesperinas, M. & Saenz, J.J. Optical forces from an evanescent wave on a magnetodielectric small particle. *Opt. Lett.* **35**, 4078–4080 (2010).
30. Bliokh, K.Y. & Nori, F. Transverse spin of a surface polariton. *Phys. Rev. A* **85**, 061801(R) (2012).
31. Fedorov, F.I. To the theory of total reflection. *Doklady Akademii Nauk SSSR* **105**, 465–468 (1955) [translated and reprinted in *J. Opt.* **15**, 014002 (2013)].
32. C. Cohen-Tannoudji, J. Dupont-Roc, and G. Grynberg, *Atom-photon interactions: basic processes and applications* (Wiley, New York, 1992)
33. A. Canaguier-Durand, J.A. Hutchison, C. Genet, and T.W. Ebbesen, Mechanical separation of chiral dipoles by chiral light, *New J. Phys* **15**, 123037 (2013).
34. Ashkin, A. & Gordon, J.P. Stability of radiation-pressure particle traps: an optical Earnshaw theorem. *Opt. Lett.* **8**, 511–513 (1983).
35. Chaumet, P.C. & Nieto-Vesperinas, M. Time-averaged total force on a dipolar sphere in an electromagnetic field. *Opt. Lett.* **25**, 1065–1067 (2000).
36. Ruffner, D.B. & Grier, D.G. Comment on “Scattering forces from the curl of the spin angular momentum of a light field”. *Phys. Rev. Lett.* **111**, 059301 (2013).
37. Canaguier-Durand, A., Cuche, A., Cyriaque, G. & Ebbesen, T.W. Force and torque on an electric dipole by spinning light fields. *Phys. Rev. A* **88**, 033831 (2013).
38. Bohren, C.F. & Huffman, D.R. *Absorption and Scattering of Light by Small Particles* (Wiley, 1983).
39. Nieto-Vesperinas, M., Saenz, J.J., Gomez-Medina, R. & Chantada, L. Optical forces on small magnetodielectric particles. *Opt. Express* **18**, 11428–11443 (2010).
40. Bekshaev, A.Y. Subwavelength particles in an inhomogeneous light field: Optical forces associated with the spin and orbital energy flows. *J. Opt*. **15**, 044004 (2013).
41. Almaas, E. & Brevik, I. Radiation forces on a micrometer-sized sphere in an evanescent field. *J. Opt. Soc. Am. B* **12**, 2429–2438 (1995).
42. M. Nieto-Vesperinas, P.C. Chaumet, and A. Rahmani, Near-field optical forces, *Phil. Trans. R. Soc. Lond. A* **362**, 719 (2004).
43. S. Chang, J.T. Kim, J.H. Jo, and S.S. Lee, Optical force on a sphere caused by the evanescent field of a Gaussian beam; effects of multiple scattering, *Opt. Commun*. **139**, 252 (1997).
44. M. Šiler and P. Zemánek, Parametric study of optical forces acting upon nanoparticles in a single, or a standing, evanescent wave, *J. Opt*. **13**, 044016 (2011).
45. Kawata S. & Tani, T. Optically driven Mie particles in an evanescent field along a channeled waveguide. *Opt. Lett.* **21**, 1768–1770 (1996).
46. Volpe, G., Quidant, R., Badenes, G. & Petrov, D. Surface plasmon radiation forces. *Phys. Rev. Lett.* **96**, 238101 (2006).
47. Gaugiran, S., Getin, S., Fideli, J.M. & Derouard, J. Polarization and particle size dependence of radiative forces on small metallic particles in evanescent optical fields. Evidences for either repulsive or attractive gradient forces. *Opt. Express* **15**, 8146–8156 (2007).
48. Wang, K., Schonbrun, E. & Crozier, K.B. Propulsion of gold nanoparticles with surface plasmon polaritons: evidence of enhanced optical force from near-field coupling between gold particle and gold film. *Nano Lett.* **9**, 2623–2629 (2009).
49. Yang, A.H.J., Lerdsuchatawanich, T. & Erickson, D. Forces and transport velocities for a particle in a slot waveguide, *Nano Lett.* **9**, 1182–1188 (2009).